

pubs.acs.org/crystal Article

Time-Resolved Cooperative Motions in the Solid-State Dehydration of Thymine Hydrate

Taylor A. Watts, Elizabeth K. Miehls, and Jennifer A. Swift*



Cite This: Cryst. Growth Des. 2020, 20, 7941–7950



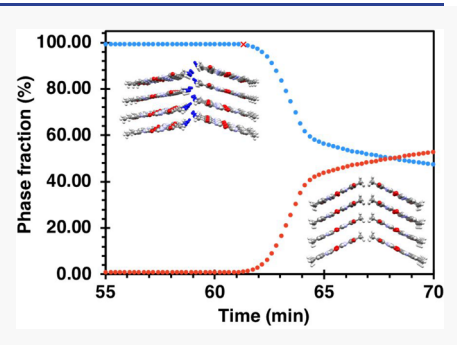
ACCESS

Metrics & More

Article Recommendations

Supporting Information

ABSTRACT: Many organic compounds can exist in hydrated and anhydrous crystalline forms, each of which exhibits its own different set of physical properties. This makes dehydration—rehydration processes an important class of solid-state reactions; yet, the molecular-level mechanisms and cooperative motions which govern such transformation in molecular solids have been notoriously difficult to establish. Here using time-resolved synchrotron X-ray powder diffraction (sPXRD) and other methods, we identify a number of early subtle changes in thymine hydrate (TH) which set its trajectory for the formation of anhydrous products. An early cooperative "morning stretch" motion, characterized by a coordinated increase in the interlayer separation and angular rotation, was observed prior to the appearance of the first major anhydrous phase, Td₁. Kinetic analyses indicated the overall solid-state reaction



proceeds via a one-dimensional diffusion mechanism with an E_a = 115–122 kJ/mol. At temperatures \geq 45 °C, solid state dehydration yielded mixtures of Td₁ and a second major anhydrous phase, Td₂. Multiphase refinement of sPXRD data proved that Td₂ is formed via two distinct routes—either directly due to water loss from TH or via the polymorphic transformation of Td₁. Heating above \sim 180 °C yielded Td₂ as the major product. A limited number of weak diffraction peaks evidence the presence of a third transient form, Td*, which also converts to Td₂. The time-resolved methods used here illustrate that solid-state dehydration even in a seemingly simple molecular hydrate system involves a significantly more complex set of coordinated molecular motions and solid—solid transformations than originally thought. The ability to glean a more complete picture of the cooperative motions that occur during water loss from soft crystalline hydrates is an important step in the development of a deeper understanding of this important class of materials.

■ INTRODUCTION

Water is ubiquitous in the manufacturing, processing, and storage of molecular materials. It is therefore not surprising that molecular hydrates are frequently encountered. 1-5 The relative stability of a crystalline hydrate compared to potential anhydrous forms depends on internal as well as external environmental factors. Since hydrated and anhydrous forms exhibit different physical properties (e.g., solubility and bioavailability), it is important ensure that the external conditions under which they are maintained do not allow for transformations between these different solid-state forms. On the other hand, the intentional dehydration of hydrates can be used as a means to create novel anhydrous crystalline forms that may not be accessible directly from solution crystallization.6-11 Regardless of whether the goal is to prevent or encourage solid state dehydration reactions, our ability to predict them is limited by an incomplete understanding of the molecular-level mechanisms by which these processes occur.

Investigations of solid-state dehydration typically employ a range of analytical tools such as thermogravimetric analysis (TGA), differential scanning calorimetry (DSC), hot stage microscopy, and X-ray diffraction on single crystals and/or powders. Thermal analyses can establish compositional changes as a function of time and/or temperature, but little

insight into the structural changes or molecular rearrangements that occur in the solid during dehydration. Diffraction methods provide better insight into structural changes; however, data collection times on conventional powder X-ray instruments are typically slower than what is needed to capture the subtle and dynamic structural changes which occur in real time. Recent advances in time-resolved synchrotron powder X-ray diffraction (sPXRD) enable the rapid collection of high resolution data under controlled environmental conditions. This makes it an ideal technique to study temporal structural changes associated with solid-state form changes, ^{12,13} though to date such methods have been applied to a relatively limited number of dehydration studies on minerals ^{14–17} and other molecular hydrates. ^{18–20}

As one of the four DNA nucleobases and a component of several active pharmaceutical ingredients used in the treatment

Received: August 31, 2020 Revised: November 5, 2020 Published: November 19, 2020





Table 1. Solid State Reaction Models and Integral Expressions Used for Kinetic Analyses^{27,28}

dehydration models	integral equation $g(\alpha) = kt$		
Nucleation and Growth			
1D growth of nuclei (A2) (Avrami–Erofeyev equation, $n = 2$)	$(-\ln(1-\alpha))^{0.5}$		
2D growth of nuclei (A3) (Avrami–Erofeyev equation, $n = 3$)	$(-\ln(1-\alpha))^{1/3}$		
3D growth of nuclei (A4) (Avrami–Erofeyev equation, $n = 4$)	$(-\ln(1-\alpha))^{1/4}$		
random nucleation (P1) (Prout-Tompkins equation)	$\ln(\alpha/(1-\alpha)) + e^{\alpha}$		
Power law $(n = 1/2)$ (P2)	$lpha^{1/2}$		
Power law $(n = 1/3)$ (P3)	$lpha^{1/3}$		
Power law $(n = 1/4)$ (P4)	$lpha^{1/4}$		
Geometrical Contraction			
2D phase boundary (R2) (contracting area)	$(1-(1-\alpha)^{1/2}$		
3D phase boundary (R3) (contracting volume)	$1-(1-\alpha)^{1/3}$		
Diffusion			
1D diffusion (D1)	$lpha^2$		
2D diffusion (D2)	$(1-\alpha)*(\ln(1-\alpha))+\alpha$		
3D diffusion (D3) (Jander equation)	$(1-(1-\alpha)^{1/3})^2$		
3D diffusion (D4) (Ginstling-Brounshtein equation)	$(1-(2/3)*\alpha)-(1-\alpha)^{2/3}$		
Reaction Order			
zero-order (R1)	α		
first-order (F1)	$-\ln(1-\alpha)$		
second-order (F2)	$(1/(1-\alpha))-1$		
third-order (F3)	$(1/2)*(((1-\alpha)^{-2})-1)$		

of diseases ranging from HIV to Hepatitis B, 21,22 investigations of thymine...water interactions are arguably important. Solid state studies on thymine hydrate (TH) date back to its first structure report over a half century ago (refcode: THYMMH).²³ In the 1980s, Perrier and Byrn²⁴ showed with hot stage microscopy that single crystal dehydration of TH was highly anisotropic, with the fastest water loss occurring along the one-dimensional water channel direction (c-axis). A more recent 2016 study by Braun et al.²⁵ examined TH dehydration with a more diverse array of experimental techniques including DSC, TGA, PXRD, IR and Raman spectroscopy, and dynamic vapor sorption. Additional experimentally accessible anhydrous polymorphs were identified and characterized in this work. Using computational methods, they also found that the maximum water occupancy of the one-dimensional channels is ~80%, which helped to explain some unusual results seen in an earlier computational study of molecular hydrates.²⁶ Importantly, potential anhydrous thymine polymorphs were generated through crystal structure prediction methods.

In the current work, we demonstrate how time-resolved sPXRD methods afford unprecedented insight into the mechanistic aspects and time-resolved structural changes that occur throughout the solid-state dehydration of TH over a wide temperature range. Time-resolved synchrotron powder X-ray diffraction studies performed at the Advanced Photon Source beamline 17-BM-B revealed a number of subtle changes in the TH lattice which precede the formation of anhydrous thymine and led to the identification of at least three anhydrous products. When taken in combination with TGA kinetic studies, this approach provides the most detailed molecular-level insight into the subtle molecular motions that occur during dehydration of this classic hydrate system.

■ EXPERIMENTAL SECTION

Sample Preparation and Characterization. Anhydrous thymine was obtained from Aldrich (\geq 99%) and used as received. Elga Purelab Flex purification system was used to produce ultrapure 18.2 MOhm water for all growth solutions. Supersaturated aqueous thymine solutions (5-6 mg/mL) were prepared in 1 dram vials and

placed in the refrigerator (4 °C). Crystals began to appear after ${\sim}10$ h. TH single crystals grew as elongated (010) plates bounded by medium (110) or (011) faces, with typical dimensions of 0.5 \times 0.15 \times 0.1 mm.

Optical micrographs were obtained on an Olympus BX-50 polarizing microscope fitted with a Lumenera Xfinity 2.0 camera attachment and Xfinity Analyze software (Lumenera, Ontario). Hot stage microscopy was accomplished with an HCS302 optical hot-stage (INSTEC, Inc., Boulder, CO). Single crystal and powder X-ray diffraction (PXRD) data were collected using a DUO Apex X-ray diffractometer (Cu K α radiation, 50 kV, 30 mA current). PXRD data were obtained at room temperature over $2\theta = 5-40^{\circ}$ in Kapton capillaries (Cole-Parmer). These data were integrated using APEX-2 software and analyzed using Panalytical X'Pert Highscore Plus software.

Thermal Analysis and Kinetic Analysis. TH dehydration was investigated with a TA Instruments differential scanning calorimeter (DSC) Q200 or Q25, each equipped with a cooling system. Dehydration experiments using DSC were performed with 3.0 mg samples in hermetically sealed aluminum pans at 5.0 °C/min over the temperature range 25–120 °C. Thermogravimetric Analysis (TGA) data were obtained on a TA Instruments SDT Q600 or Q50 instrument (New Castle, DE) using a nitrogen flow rate of 50 mL/min. All experiments used 3.0–5.0 mg of as-grown TH crystals in either open 100 μ L platinum or 90 μ L aluminum pans (TA Instruments).

Isothermal dehydration experiments using TGA were performed in triplicate at 35, 45, and 50 °C. The fraction dehydrated, α , was determined from the % mass loss at each data point relative to the total experimental wt % loss (on average 9.4(4) wt %) according to eq 1.

$$\alpha = \frac{w_0 - w_t}{w_0 - w_f} \tag{1}$$

The linear portions (0.25 < α < 0.9) of the isothermal TGA curves were then subjected to kinetic analyses following established model-based and model-free methods. For model-based analyses, data were fit to each of the solid-state models in Table 1 which have the general form

$$\frac{\mathrm{d}\alpha}{\mathrm{d}t} = Ae^{-(E_a/RT)}f(\alpha) = k(T)f(\alpha)$$
 (2)

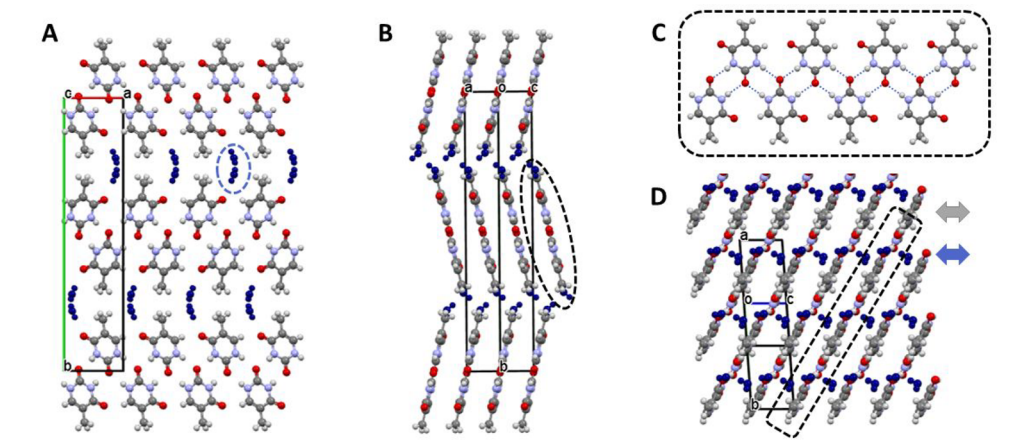


Figure 1. Multiple views of the TH structure. (A) View down the c-axis. One water channel is indicated by the dashed blue circle. (B) View down the [101] thymine ribbon direction where one thymine ribbon is identified by the dashed black oval. Each ribbon is tilted by $\sim 12^{\circ}$ relative to the b-axis. (C) Hydrogen bonding between thymine molecules creates a nonpolar ribbon. (D) View $\sim 12^{\circ}$ off the b-axis helps to visualize the relative arrangement of these features. Water channels and π -stacking (blue and gray arrows) run in parallel while the hydrogen bonded thymine tapes traverse many water channels within a (010) layer.

where A is the pre-exponential or frequency factor, $E_{\rm a}$ is the activation energy (J/mol), R is the gas constant (8.314 JK⁻¹ mol⁻¹), k(T) is the rate constant, and $f(\alpha)$ is the reaction model in its differential form. The kinetic models were assessed based on the correlation coefficient (R^2) and the standard deviation in the slope of the regression line ($S_{\rm m}$).

Time-Resolved Synchrotron Powder X-ray Diffraction (sPXRD). All synchrotron powder X-ray diffraction data were collected at the Advanced Photon Source (APS) beamline 17-BM-B. Experiments had an X-ray beam energy of \sim 27 keV (λ = 0.39433 Å, 0.45212 or 0.24141) and a beam size of 300 μ m. The beamline uses a Si (311) monochromator, a PerkinElmer a-Si Flat Panel PE1621 area detector, and the Oxford Cryosystems Cryostream 700+. Samples were ground in the mother liquor, loaded wet into 1.1 mm OD Kapton capillary (Cole-Parmer), stoppered with glass wool, and then placed in a flow cell designed for in situ experiments.²⁹ Samples were maintained under a constant He gas flow at 5 mL/min (essentially RH = 0%) and rocked at 15° throughout the data collection. With an exposure time of 1-2 s per image (summed over 10 images), this experimental setup allowed a high Q-range sPXRD pattern to be collected every ~13-20 s. Dehydration experiments were performed at constant temperature (22-57 °C) and under nonisothermal heating (3-10 °C/min) conditions. High-humidity experiments (RH ~ 70%) were also performed under constant He gas flow of 5 mL/min through a water bubbler. GSAS-II software³⁰ was used for image processing and integration.

sPXRD patterns were refined using TOPAS-V6 software.³¹ TH, Td₁, and Td₂ structures were determined through Rietveld refinement using the fundamental parameters approach. The TH structure was determined from refinement of PXRD data collected at 22, 27, 45, 50, and 57 °C. An experimental structural model for Td₁ was determined from 27 °C isothermal data through multiphase refinement (the final sPXRD pattern contained a small amount of TH) using a computed starting model (32_113) reported in ref 25. Refined parameters included background terms (chebychev, six terms total), zero error, unit cell parameters, and crystallite size and strain. The rigid body and associated atomic positions were fixed for TH and refined for Td₁. The final Td₁ structure had a $R_{\rm wp}$ = 15.39% and a goodness-of-fit (GOF) = 6.42.

An experimental structural model for Td_2 was determined by heating a TH sample at 10 °C/min to a maximum temperature of 100 °C. The sample (a mixture of Td_1 and Td_2) was subsequently cooled to room temperature. Once exposed to RH \sim 70%, the phase fraction of Td_1 was slowly reduced resulting in a powder pattern that was majority Td_2 with only a small amount of TH phase impurity. Td_2 was indexed to a C2 cell and subjected to Pawley refinement, with

simulated annealing used for structure solution. Refined parameters included background terms (chebychev, six terms total), zero error, unit cell parameters, and crystallite size and strain. The refinement improved slightly when the structural model included ${\sim}3\%$ TH as a phase impurity. The final Rietveld refinement gave a $R_{wp}=13.38\%$ and a GOF = 5.46.

RESULTS AND DISCUSSION

Thymine Hydrate (TH) Structure. TH is a classic hydrate system in which one-dimensional channels along the $\pm c$ -axis are occupied by water molecules. Several views of the TH structure are presented in Figure 1, with water molecules shown in blue for clarity. Figure 1a is a view down the channel (c-axis) in which water molecules hydrogen bond to one another $(O_w \cdots O_w = 2.55 \text{ Å})$ as well as to the O4 atoms of thymine molecules $(O_w \cdot \cdot \cdot O4 = 2.84 \text{ Å})$. The water channels are delineated on two sides by the 5-methyl groups of thymine, and above and below by the O4 and C6-H groups. Thymine molecules assemble into planar hydrogen bonded ribbons which orient along [101]. In Figure 1b, TH is viewed down the ribbon direction, which serves to highlight their planarity and parallel alignment, which creates close packed (3.8 Å repeat) π stacks in the c-axis direction. The hydrogen bonding motif within each ribbon via $O2\cdots H-N3$ ($O2\cdots N3 = 2.84$ Å) is nonpolar (Figure 1c).

Two additional structural aspects are directly relevant to the ensuing discussion. Notably, the ribbons within each densely packed plane are tilted by $\sim\!12^\circ$ relative to the $b\text{-}\mathrm{axis}$, with the \pm sign of the tilt alternating in adjacent (010) planes. The view in Figure 1d is just slightly off the $b\text{-}\mathrm{axis}$ to illustrate the spatial relationship between the water channel (blue arrow), $\pi\text{-}\mathrm{stacking}$ (gray arrow), and thymine ribbon (dashed oval) directions. The water channels and $\pi\text{-}\mathrm{stacking}$ directions parallel one another, whereas each thymine ribbon traverses multiple water channels within the (010) plane.

Thermal Analysis and Dehydration Models. The properties of TH were first investigated using hot stage microscopy and DSC, yielding results consistent with previous studies. Hot stage microscopy experiments confirmed highly anisotropic dehydration, with the fastest rates occurring along the $\pm c$ -axis (Figure S1). Dehydration of single crystals yielded polycrystalline material which retains the same original

plate morphology. Differential scanning calorimetry experiments showed TH dehydration at 54.4(7) °C (95% CI, n > 5) when performed in hermetically sealed pans at a heating rate of 5.0 °C/min (Figure S2). Thermogravimetric analysis (TGA) showed an average weight loss of 9.4(4) wt % (95% CI, n > 3), which corresponds to a water occupancy of 0.72(5) (95% CI, n > 3).

Isothermal TGA data at 35 °C, 45 and 50 °C were collected in triplicate and the extent of the reaction, expressed as the fraction of TH converted (α) , was calculated from the change in weight with time (Figure 2). In some cases, a small fraction

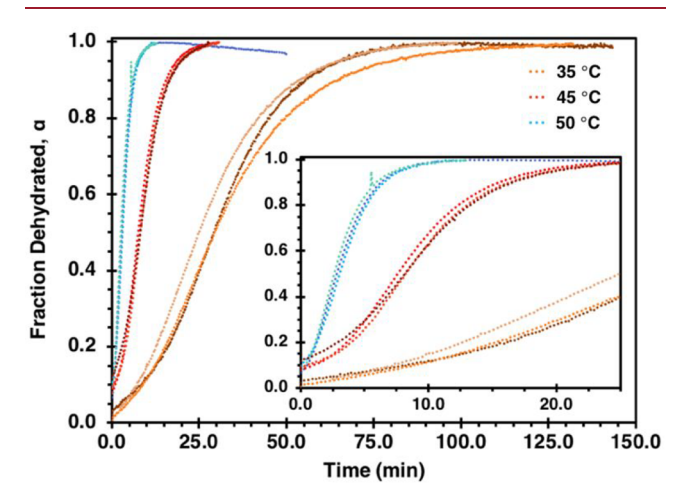


Figure 2. TGA curves obtained in triplicate for isothermal dehydration of TH at 35 °C (orange), 45 °C (red), and 50 °C (blue). The inset is a close-up of the region from 0–22.5 min.

of TH begins to dehydrate prior to reaching the target isothermal temperature, but good linearity was generally observed between 0.25 < α < 0.9. The TGA data were then subjected to kinetic analyses following established model-based and model-free methods. $^{27,28,32-35}$

Model-based analyses, which are useful in identifying the most probable rate limiting step in the solid-state reaction, involved fitting the linear region of the isothermal TGA curves in Figure 2 to the solid-state dehydration models (e.g., nucleation and growth, geometrical contraction, diffusion, and reaction order) listed in Table 1. The quality of the fit to each model was evaluated based on the correlation coefficient (R^2) and the standard deviation in the slope of the regression line (S_m) . At both 35 and 50 °C, the one-dimensional diffusion mechanism (D1) model provided the highest correlation R^2 = 0.9980 and 0.9971, respectively. Data at 45 °C had an equally good fit for this model and a one-dimensional growth of nuclei (A2) model. For R^2 results from all models, see Table S1. Dehydration of TH via a one-dimensional diffusion mechanism is also consistent with hot stage microscopy which qualitatively showed highly anisotropic dehydration along the c-axis.

Kinetic analyses with model-free methods allowed the activation energy $(E_{\rm a})$ to be determined at fixed points along the reaction coordinate without any additional mechanistic assumptions. Typically, when a constant $E_{\rm a}$ over the experimental time period is observed, it is assumed that the mechanism does not change throughout the reaction. When time-dependent changes in $E_{\rm a}$ are observed, more than one more reaction model may be needed to accurately describe the dehydration mechanism. Both Friedman³⁶ and Standard^{34,35}

analysis methods yielded a similar steady $E_{\rm a}=115-122~{\rm kJ/mol}$ throughout the dehydration reaction (Figure S3). On the basis of these thermal data analyses, one would surmise that TH dehydration occurs via a consistent one-step mechanism throughout the course of the reaction.

Time-Resolved Synchrotron PXRD (sPXRD). Monitoring TH dehydration under similar isothermal conditions using time-resolved synchrotron powder X-ray diffraction allowed for the tracking of structural changes that occur over time. All sPXRD data were collected at the Advanced Photon Source beamline 17-BM-B. TH samples were hand ground in a small amount of growth solution and loaded into capillaries which were placed in a climate-controlled flow cell (Figure S4). Dehydration experiments were run under isothermal conditions (22, 27, 45, 50, and 57 °C) under a constant He gas flow of 5 mL/min (essentially a 0% RH). Additional experiments in which TH was heated from 22 to 222 °C at rates of 1, 3, 5, and 10°/min were also performed. Diffraction data were collected using an exposure time of 1-2 s per image with summation over 10 images, thereby enabling a high resolution sPXRD pattern to be collected approximately every 13-23 s. Rietveld refinement of the sPXRD data allowed for examination of early structural changes in TH, the extraction of reaction kinetics based on changing phase compositions over time, and structure determination of the anhydrous products.

Compared to the TGA kinetic analyses which indicated TH dehydration occurred via a one-step mechanism, isothermal time-resolved sPXRD experiments revealed a significantly more complex set of interrelated structural changes. Depending on the thermal conditions, each of the sPXRD dehydration experiments yielded either one or two major dehydration products, which we refer to as Td_1 and Td_2 . In some experiments, a small number of unassignable low intensity diffraction lines indicated the presence of a third as yet undetermined phase which we refer to as Td^* .

Our detailed description of the structural changes that occur begins with an analysis of dehydration at low temperatures which yielded primarily Td_1 , including a discussion of counterintuitive structural changes that occur in TH prior to the appearance of this dehydration product. Dehydration at higher temperatures and under temperature-ramping conditions which yielded mixtures of Td_1 and Td_2 are then discussed. A summary of the times and/or temperatures at which each anhydrous product appeared under all thermal conditions is found in Table S2.

Structural Changes in TH Before Anhydrous Product Formation. Sequential refinement of time-resolved sPXRD patterns obtained from isothermal dehydration at 22-27 °C revealed that TH undergoes subtle but highly reproducible structural changes before the appearance of anhydrous product phases. Representative data collected over a ~ 15 min time period nearly an hour after initiating a 27 °C isothermal experiment are shown in Figure 3. The plots, made from the refinement of 70 different sPXRD patterns, track the TH unit cell parameters at each time point in the reaction and the phase fraction of TH in the sample. The vertical dashed red line in each corresponds to the first sPXRD pattern showing weak diffraction intensity due to product phase. Many subtle changes in the TH unit cell prior are observed prior to the emergence of dehydrated phases, including a small decrease in its volume (0.26%). The decrease in volume suggests the TH lattice can tolerate some limited amount of early water loss before collapsing to Td₁.

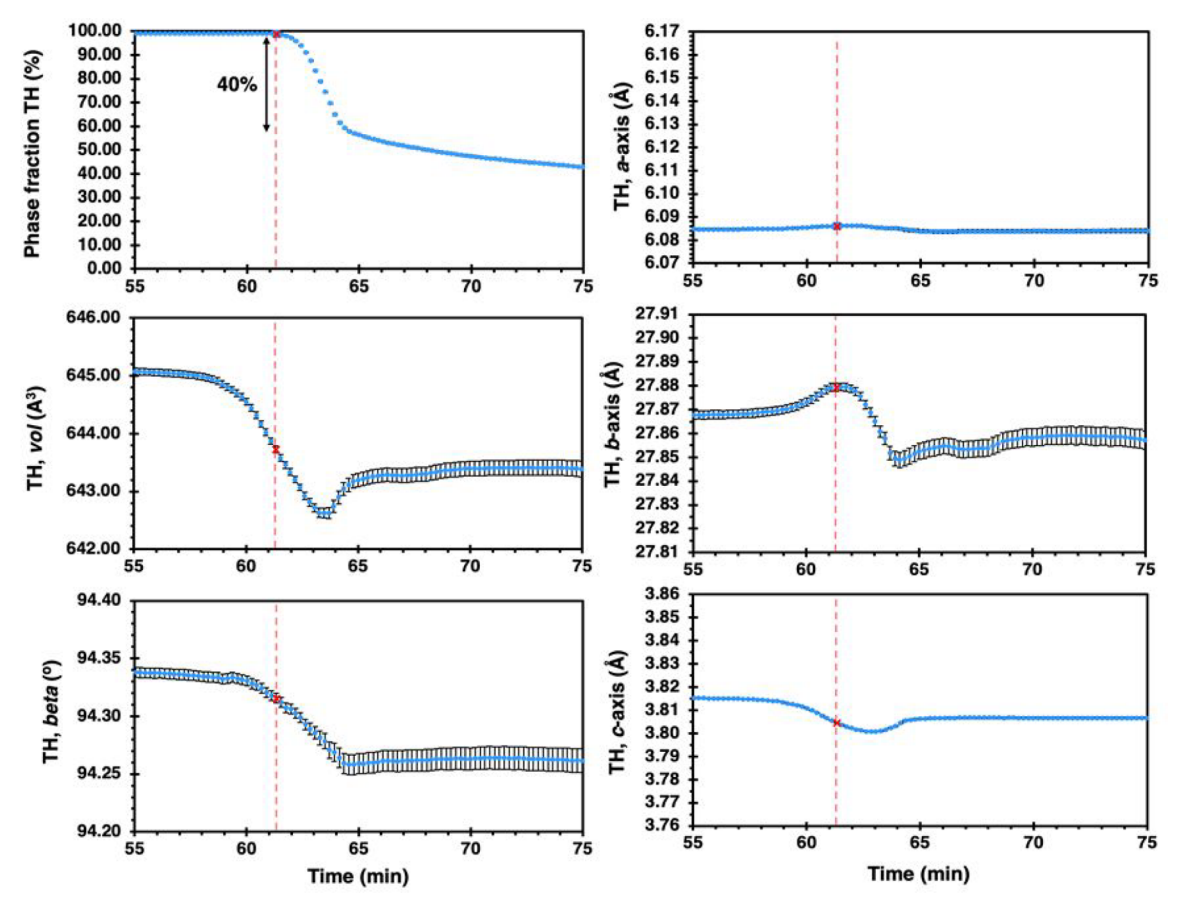


Figure 3. Unit cell parameters obtained from sequential refinement of sPXRD patterns of TH maintained at 27 $^{\circ}$ C before the appearance of Td₁. The small decrease in cell volume suggests that the TH lattice can tolerate some water loss prior to collapse. The *b*-axis undergoes an expansion (blue arrow) before it contracts. The same trends are observed in isothermal data sets collected at higher temperatures.

The a-axis and c-axis cell parameters which define the dense two-dimensional layers of π -stacked ribbons showed comparatively little change during this time interval. Most surprising was the fact that over several minutes the b-axis of TH undergoes an expansion before later contracting. This expansion was consistently observed in all replicate experiments performed at 22 and 27 °C. Anisotropic expansion has been observed in other channel hydrates, though typically in systems which can accommodate variable stoichiometries and under high humidity conditions where increases along a given axis are attributed to water uptake. The water uptake are under flowing He gas, an essentially 0% RH environment, where water uptake is not likely.

Since even small amounts of water loss create void space in the interlayer region, one would more likely expect the interlayer separation to be *reduced*. Though the initial expansion along the *b*-axis at 22-27 °C seems almost counterintuitive, its reproducibility indicates it is critical to the formation of anhydrous product. Notably, the anhydrous product appears only *after* the *b*-axis of TH reaches it maximum value, at which point the phase fraction of TH in the sample drop precipitously. A slight but steady change in the β -angle is also observed during this time interval. In what must be an effort to presumably minimize the overall lattice energy, the combination of *b*-axis expansion and decrease in β -angle reflect a coordinated "morning stretch" type of lattice motion

which facilitates the translation and/or rotation of layers at the (010) interface.

Interestingly, isothermal experiments performed at higher temperatures (45, 50, and 57 °C) do not show a b-axis expansion prior to product formation, though this may be in part due to thermal expansion effects. TH unit cell parameters determined from 27, 45, 50, and 57 °C data sets showed a comparatively larger increase in the a and c-axes at elevated temperatures relative to the b-axis (Figure 4). The increased cell volume at higher temperatures may obviate the need to expand along the b-axis in order to optimize the layer registry.

Low Temperature Isothermal Dehydration to Td_1 . Although data indicate TH is able to withstand some fractional water loss, at some point the TH lattice becomes sufficiently unstable and collapses to anhydrous forms. At the lowest isothermal temperatures between 22 and 27 °C, TH transforms primarily to Td_1 . As discussed, the onset occurs when the maximum b-axis length is reached, after which \sim 40% of TH converts to Td_1 in a matter of only a few minutes. After this initial rapid conversion, the rate at which TH subsequently converts to Td_1 is much slower. Even after 9 h of data collection, the reaction does not fully go to completion at 27 °C, as evidenced by the persistence of low intensity peaks corresponding to residual amounts of TH in the sPXRD patterns.

The structure of Td_1 was determined through Rietveld refinement of sPXRD data using TOPAS-V6 in combination with computed structures generously shared by Dr. Doris

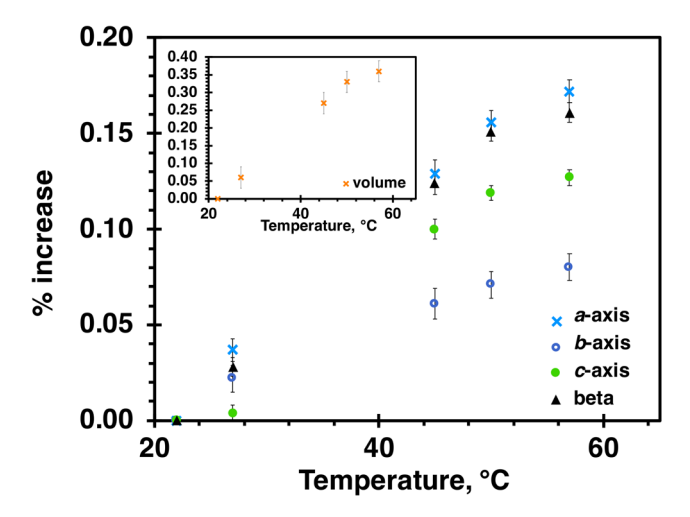


Figure 4. Thermal expansion of TH unit cell parameters at 27, 45, 50, and 57 compared to 22 $^{\circ}$ C. The values at each temperature are an average of at least 10 sPXRD patterns refined at each temperature. The inset graph plots the cell volume changes over the same temperature range.

Braun (Figure S5). Td_1 was confirmed to have the same anhydrous structure as what she referred to as "AH D" in ref 25. Comparison of TH and Td_1 structures determined from 27 °C (300 K) sPXRD patterns shows that the two structures are topologically similar despite an 11.6% reduction in the unit cell volume (Figure 5, Table 2). This suggests a high level of concerted molecular motion in the TH to Td_1 transformation and a continuation of the early structural changes in TH.

The packing within the dense two-dimensional layers in the ac plane of TH and Td_1 is identical, with only minor changes seen in the repeat distance along each hydrogen bonded ribbon (1.5% lower in Td_1) and the separation between the π -systems of adjacent ribbons (0.6% lower in Td_1). The most significant dimensional change in going from TH to Td_1 is seen in the b-axis which decreases by 16.5% (from 27.86 to 23.25 Å). Since water loss from TH along the c-axis channels necessarily creates void space between adjacent layers, a decrease in the (010) layer separation was not unexpected. Some of the layer compression can also be attributed to a significant increase in the tilt angle between the hydrogen bonded ribbons and the b-axis (from 12.00 in TH to 24.69° in

 Td_1). Presumably, this enables a denser packing of layers, as evidenced by the closer methyl—methyl contacts across the layer interface in Td_1 compared to TH. That the (010) layers would initially increase their separation in order to ultimately access this more compact anhydrous phase illustrates that the cooperative trajectories for solid state reactions are both subtler and more complex than previously thought. The early "morning stretch motions" observed in TH prior to the formation of Td_1 can be viewed as a critical precursor which allows methyl groups in adjacent layers to slide past one another in order to ultimately access a denser phase.

Dehydration to Mixtures of Td_1 and Td_2 . Isothermal heating of TH at 45, 50, and 57 °C yielded mixtures of Td_1 and a second major anhydrous phase, Td_2 . The phase fraction of each component throughout the reaction progress was determined from multiphase refinement of hundreds of sPXRD patterns. Plots of the changing phase composition over time illustrate several key points (Figure 6). First, the rate at which anhydrous products are formed increases at higher temperatures. Second, the Td_1 formation rate is faster than that of Td_2 . Third, increases in the temperature yielded a higher fraction of Td_2 in the final dehydration product. For example, dehydration at 45 and 57 °C yielded final Td_1/Td_2 product ratios of $\sim 3.8:1$ and 2.5:1, respectively.

The increased fraction of Td_2 generated from dehydration at higher isothermal temperatures suggested two possible interpretations which are not mutually exclusive. Assuming TH can convert to both of the major dehydration products directly, if the activation energy (E_a) for the TH to Td_2 reaction is higher than the E_a for the TH to Td_1 reaction, elevated temperatures should show a relative rate enhancement favoring Td_2 thereby increasing its fraction in the product mixture. Isothermal experiments showed that Td_1 was the only major dehydration product when TH was heated at 22-27 °C, and the first major product to appear when TH was heated at 45 °C. In isothermal experiments performed at 50 or 57 °C, Td_2 appeared prior to Td_1 . This confirms a direct pathway from TH to both products and is consistent with a lower E_a for the conversion of TH to Td_1 .

Alternatively, if Td₁ undergoes a polymorphic transformation to Td₂, one would expect a larger fraction of Td₂ to be present at temperatures above the phase transition temperature. Temperature ramping experiments performed to

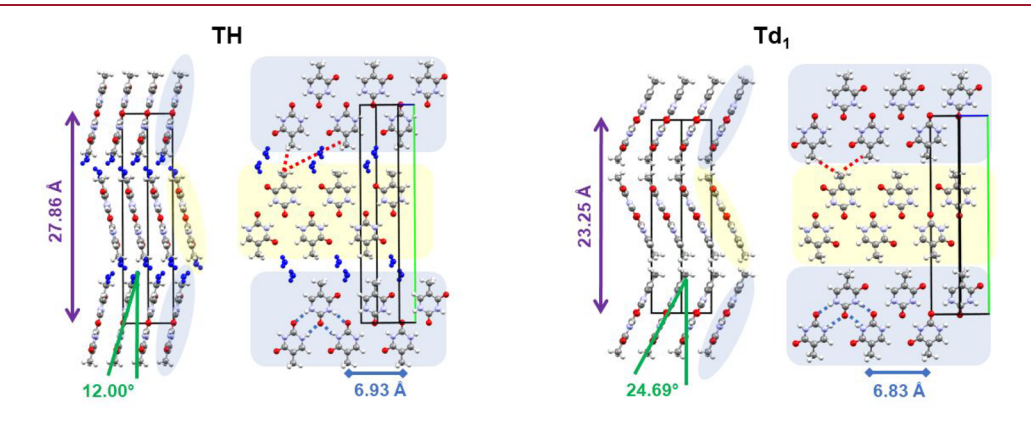


Figure 5. Side by side comparison of TH and Td_1 structures viewed along $[10\overline{1}]$ and $[\overline{1}01]$ directions illustrate the similarities and differences in the two lattices. Blue dashed lines illustrate H-bonding within the ribbons. Red dashed lines indicate the closest C···C distances between methyl groups which are 4.27 and 7.31 Å in TH and 4.12 and 4.32 Å in Td_1 . For clarity purposes, only a small number of hydrogen bonds and interlayer contacts are shown.

Table 2. Crystallographic Information for TH, Td₁, and Td₂ Determined from Refinement of sPXRD Data^a

crystallographic Info.	TH (THYMMH)	TH	Td_1	Td_2
formula	$C_5H_6N_2O_2\cdot 0.80\ H_2O$	$C_5H_6N_2O_2 \cdot 0.80H_2O$	$C_5H_6N_2O_2$	$C_5H_6N_2O_2$
temperature	RT	27 °C	27 °C	22 °C
space group	$P2_1/c$	$P2_1/c$	$P2_1/n$	C2
a (Å)	6.077	6.0841(3)	4.5436(11)	6.7729(7)
b (Å)	27.862	27.8635(15)	23.247(5)	6.8409(8)
c (Å)	3.816	3.81653(13)	5.4139(11)	12.843(2)
β (deg)	94.32	94.349(4)	93.88(2)	104.958(11)
vol (ų)	644.279	645.13(5)	570.5(2)	574.90(13)
characterization	XRD	sPXRD	sPXRD	sPXRD

^aFor atom positions see Supporting Information.

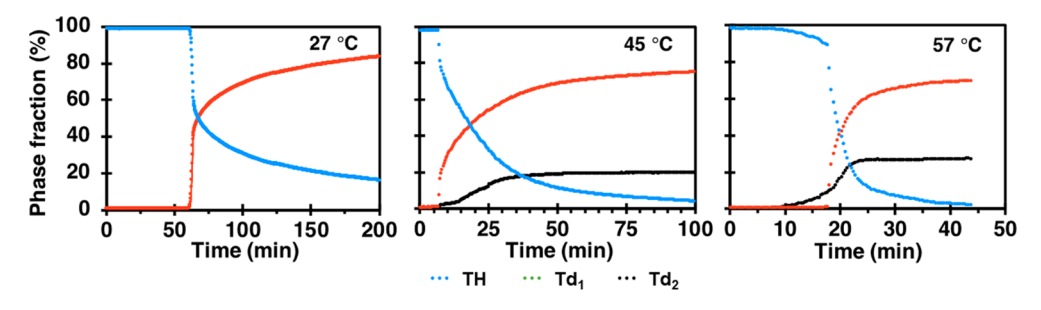


Figure 6. Changing phase compositions determined from multiphase refinement of sPXRD collected under isothermal dehydration of TH at 27, 45, and 57 $^{\circ}$ C. Dehydration at 27 $^{\circ}$ C yields only Td₁ while at higher temperatures result in two major anhydrous phases, Td₁ and Td₂. The phase fraction of Td₂ is higher at 57 than at 45 $^{\circ}$ C.

a maximum temperature of 222 °C confirmed a Td_1 to Td_2 polymorph conversion does occur. Across all temperature ramping experiments, ~ 43 °C was the lowest temperature where Td_2 was observed. This is consistent with its absence in isothermal experiments at 27 °C but appearance at 45 °C. By 100 °C, all ramping experiments resulted in the complete conversion of TH to mixtures of Td_1 and Td_2 phases. Above temperatures $\sim 172-190$ °C (depending on the heating rate) diffraction peaks correspond to Td_2 . In some experiments, lowintensity diffraction lines indicated the presence of small amounts of sublimed thymine ($T_{\rm sub}$, THYMIN02) in the sample. The contour plot in Figure 7 generated from data collected at a heating rate of 3 °C/min illustrates the initial formation of Td_1 and its later disappearance at higher temperatures.

In several in situ dehydration experiments, two additional weak diffraction peaks at Q=0.49 and $Q=0.99~{\rm \AA}^{-1}$ were observed in the sPXRD which are not ascribable to TH, Td₁ or Td₂ (Figure S6). This evidence the presence of minor amounts of a third phase in the mixture, which we refer to as Td*. Since structure solution is not possible on the basis of only two diffraction lines, the structure of Td* remains elusive. When Td* was observed, its onset temperature was typically similar to but not exactly the same as that of Td₁. In no experiment did the weak diffraction associated with Td* persist beyond the time when Td₂ appeared, suggesting that this short-lived transient phase also transforms to Td₂. This is the first experimental evidence for a third form of thymine formed via dehydration.

Structure Solution of Td₂. The structure of Td₂ was determined from sPXRD data generated from heating TH at 10 $^{\circ}$ C/min to 100 $^{\circ}$ C to yield a mixture of Td₁ and Td₂. Subsequent cooling to room temperature and exposure to RH $\sim 70\%$ yielded a final powder pattern that was majority Td₂ with some minor TH impurity. We cannot discount the

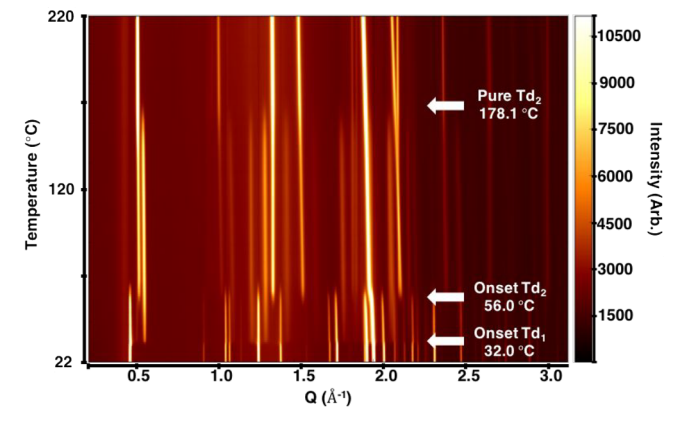


Figure 7. Contour plot constructed from 50 sPXRD patterns collected during TH dehydration when heated from 22–220 °C at 3 °C/min. Diffraction lines corresponding to Td_1 and Td_2 first appear at 32.0 and 56.0 °C, respectively. By 178.1 °C, all Td_1 has undergone a phase transformation to Td_2 .

possibility of a simultaneous transformation from Td₁ to Td₂ under high RH conditions, as the Td₁ structure has been shown to be metastable relative to other anhydrous forms in humid environments. The sPXRD data indexed to a C2 cell and was subjected to Pawley refinement, with simulated annealing used for structure solution. The final refinement yielded a structure with unit cell parameters a = 6.7729(7) Å, b = 6.8409(8) Å, c = 12.843(2) Å, $\beta = 104.958(11)^\circ$, and Vol = 574.90(13) ų and an $R_{\rm wp} = 13.38\%$ and GOF = 5.46. The Rietveld plot is shown in Figure 8. Notably, this is a different lattice than the second major form generated via TH dehydration as previously reported by Braun; however, the conditions and experimental methods used in the previous and current studies were not identical.

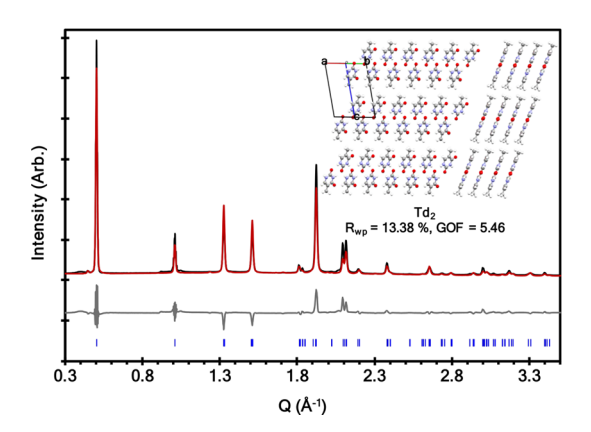


Figure 8. Rietveld plot for the solved structure of Td_2 . Observed intensity information is shown in black, modeled intensity is shown in red, and the difference pattern is shown in gray. Reflections are shown in blue tic marks.

One of the challenging aspects of modeling sPXRD data for this product stems from the fact that many experimental and computed anhydrous thymine polymorphs are polytypic (Figure S7). One Molecules can assemble into one of two different ribbon motifs (polar or nonpolar), and the orientation of ribbons within and between the two-dimensional layers can also vary (parallel or antiparallel). Ribbons in TH, Td_1 , and T_{sub} are nonpolar, whereas in Td_2 and anhydrous thymine grown from nonaqueous solution (T_{sol}) THYMIN01) have identical polar motifs. Although Td_2 and T_{sol} have identical ribbon structures, all ribbons in Td_2 align in parallel, whereas in T_{sol} the adjacent ribbons within a layer are antiparallel to achieve centrosymmetry. With similar repeating cell dimensions, the PXRD patterns of these polytypes share many of the same high intensity diffraction lines (Figure S8).

To confirm C2 was in fact the best fit and rule out other possibilities, we also refined the sPXRD data against $T_{\rm sob}$ $T_{\rm sub}$, and other models generated by previous crystal structure prediction methods. After completing multiple refinement cycles in TOPAS-V6, the C2 structure (which corresponds to computed structure #544 in ref 25) remained the best fit to the data. On the basis of the previous CSP results, Td_2 generated under these high temperature conditions is at least 6 kJ/mol higher than the global minimum. (For reference, $T_{\rm sub}$ and $T_{\rm sol}$ are both within 1 kJ/mol above the minimum.) Further information on the refinement details and alternative models tested are found in Supporting Information.

CONCLUSION

The mechanisms and cooperative lattice motions that dictate the pathway for water loss (or uptake) from molecular crystals have been difficult to establish owing to the lack of methods which enable the temporal collection of high resolution data. The results reported herein serve as a proof-of-concept that progress in time-resolved sPXRD techniques has sufficiently advanced to enable new insights into solid state reactions in this class of materials. Despite having a seemingly simple layer structure, early dehydration of TH at low temperature involves an almost counterintuitive cooperative "morning stretch" motion, a motion that helps to establish the most efficient low energy trajectory and leads directly to the first major product, Td₁. The closest analogy to these subtle structural changes may be the "breathing" motions reported in soft metal—organic framework materials (MOFs) upon adsorp-

tion/desorption of water and other guest molecules. However, the relative strength of the metal—organic units in a MOF which provide a robust but flexible porous lattice network and the interactions which determine the integrity and dimensions of water channels in organic molecular materials are quite different. In the case of TH, the time-resolved lattice changes reflect the most efficient means to respond to the changing energetic requirements at the interface between two-dimensional layers as initial water is lost. Only at the point at which no further adjustments can reasonably sustain the integrity of the TH lattice does the fast transformation to a new Td₁ lattice occur.

At higher temperatures or with faster heating rates, a second major dehydration product emerges, Td_2 , from two different solid-state precursor phases. Although the dissimilarity in the precursor and product structures does not lend itself to an analysis of cooperative molecular motions, sPXRD does provide a unique view of the reaction complexity (which was in no way apparent in microscopy or DSC/TGA studies). Compositional changes in the sample with time allow for insights into the relative kinetics and activation energies of the Td_2 versus Td_1 formation pathways to emerge. We do not yet have a sense for how ubiquitous this particular cooperative stretch type motion is in other dehydrating hydrates beyond TH, though it seems likely to be generalizable. Future studies on other crystalline hydrates with similar and/or different lattice topologies will attempt to address this point.

ASSOCIATED CONTENT

Supporting Information

The Supporting Information is available free of charge at https://pubs.acs.org/doi/10.1021/acs.cgd.0c01210.

Hot stage microscopy, TGA, synchrotron PXRD (PDF)

AUTHOR INFORMATION

Corresponding Author

Jennifer A. Swift — Department of Chemistry, Georgetown University, Washington, D.C. 20057-1227, United States; orcid.org/0000-0002-8011-781X; Email: jas2@georgetown.edu

Authors

Taylor A. Watts — Department of Chemistry, Georgetown University, Washington, D.C. 20057-1227, United States Elizabeth K. Miehls — Department of Chemistry, Georgetown University, Washington, D.C. 20057-1227, United States

Complete contact information is available at: https://pubs.acs.org/10.1021/acs.cgd.0c01210

Notes

The authors declare no competing financial interest.

ACKNOWLEDGMENTS

The authors gratefully acknowledge financial support from the National Science Foundation (DMR 1609541 and 2004435) and the Clare Booth Luce Foundation (TAW Predoctoral Fellowship). We thank Sally Price and Doris Braun for sharing with us their calculated anhydrous thymine polymorph structures in ref 45 and 25, and Andrey Yakovenko and Weiquian Xu for their assistance with collecting synchrotron data. This research used resources of the Advanced Photon Source, a U.S. Department of Energy (DOE) Office of Science

User Facility operated for the DOE Office of Science by Argonne National Laboratory under Contract No. DE-AC02-06CH11357.

REFERENCES

- (1) Griesser, U. J. The importance of solvates. In *Polymorphism in the Pharmaceutical Industry*; Hilfiker, R., Ed.; Wiley-VCH: Weinheim, 2006; pp 211–257.
- (2) Görbitz, C. H.; Hersleth, H.-P. On the inclusion of solvent molecules in the crystal structures of organic compounds. *Acta Crystallogr., Sect. B: Struct. Sci.* **2000**, *56*, 526–534.
- (3) Stahly, G. P. Diversity in Single- and Multiple-Component Crystals. The Search for and Prevalence of Polymorphs and Cocrystals. *Cryst. Growth Des.* **2007**, *7* (6), 1007–1026.
- (4) van de Streek, J.; Motherwell, S. New software for searching the Cambridge Structural Database for solvated and unsolvated crystal structures applied to hydrates. *CrystEngComm* **2007**, *9* (1), 55–64.
- (5) Werner, J. E.; Swift, J. A. Data mining the Cambridge Structural Database for hydrate—anhydrate pairs with SMILES strings. *CrystEngComm* **2020**, *22*, 7290.
- (6) Guo, F.; Harris, K. D. M. Structural understanding of a molecular material that is accessed only by a solid-state desolvation process: The scope of modern powder x-ray diffraction techniques. *J. Am. Chem. Soc.* **2005**, 127, 7314–7315.
- (7) Berzins, A.; Trimdale, A.; Kons, A.; Zvanina, D. On the Formation and Desolvation Mechanism of Organic Molecule Solvates: A Structural Study of Methyl Cholate Solvates. *Cryst. Growth Des.* **2017**, *17* (11), 5712–5724.
- (8) Mahieux, J.; Sanselme, M.; Coquerel, G. Access to Several Polymorphic Forms of (±)-Modafinil by Using Various Solvation—Desolvation Processes. *Cryst. Growth Des.* **2016**, *16* (1), 396–405.
- (9) Bhandary, S.; Chopra, D. Observation of Rapid Desolvation of Hexafluorobenzene Involving Single-Crystal-to-Single-Crystal Phase Transition in a Nonporous Organic Host. *Cryst. Growth Des.* **2018**, *18* (1), 27–31.
- (10) Zhang, Q.; Mei, X. Two New Polymorphs of Huperzine A Obtained from Different Dehydration Processes of One Monohydrate. *Cryst. Growth Des.* **2016**, *16* (6), 3535–3542.
- (11) Bhardwaj, R. M.; McMahon, J. A.; Nyman, J.; Price, L. S.; Konar, S.; Oswald, I. D. H.; Pulham, C. R.; Price, S. L.; Reutzel-Edens, S. M. A Prolific Solvate Former, Galunisertib, under the Pressure of Crystal Structure Prediction, Produces Ten Diverse Polymorphs. J. Am. Chem. Soc. 2019, 141 (35), 13887–13897.
- (12) Leineweber, W.; Mittenmeijer, E. J. Kinetics of Phase Transformations and of Other Time-Dependent Processes in Solids Analyzed by Powder Diffraction. In *Modern Diffraction Methods*; Mittenmeijer, E. J., Welzel, U., Eds., Wiley: Hoboken, New Jersey, 2013.
- (13) Harris, K. D. M.; Williams, P. A., Structure Determination of Organic Molecular Solids from Powder X-Ray Diffraction Data: Current Opportunities and State of the Art. In *Advances in Organic Crystal Chemistry*; Tamura R, M. M., Ed.; Springer: Tokyo, 2015.
- (14) Wang, D.; Yi, L.; Huang, B.; Liu, C. High-temperature dehydration of talc: a kinetics study using in situ X-ray powder diffraction. *Phase Transitions* **2015**, 88 (6), 560–566.
- (15) Liu, C.; Zhang, R.; Shen, K.; Liu, T.; Wen, W.; Wang, D. An IN SITU Kinetic Study of the Dehydration of Brucite Using Synchrotron X-ray Powder Diffraction. *Can. Mineral.* **2018**, *56* (1), 101–108.
- (16) Luo, J.; Martinez-Casado, F. J.; Balmes, O.; Yang, J.; Persson, C.; Engqvist, H.; Xia, W. In Situ Synchrotron X-ray Diffraction Analysis of the Setting Process of Brushite Cement: Reaction and Crystal Growth. ACS Appl. Mater. Interfaces 2017, 9 (41), 36392—36399.
- (17) Snellings, R.; Mertens, G.; Adriaens, R.; Elsen, J. In situ synchrotron X-ray powder diffraction study of the early age hydration of cements blended with zeolitite and quartzite fines and water-reducing agent. *Appl. Clay Sci.* **2013**, *72*, 124–131.

- (18) Nunes, C.; Mahendrasingam, A.; Suryanarayanan, R. Investigation of the Multi-Step Dehydration Reaction of Theophylline Monohydrate Using 2-Dimensional Powder X-ray Diffractometry. *Pharm. Res.* **2006**, 23 (10), 2393–2404.
- (19) Fujii, K.; Aoki, M.; Uekusa, H. Solid-State Hydration/ Dehydration of Erythromycin A Investigated by ab Initio Powder X-ray Diffraction Analysis: Stoichiometric and Nonstoichiometric Dehydrated Hydrate. *Cryst. Growth Des.* **2013**, *13* (5), 2060–2066.
- (20) Boetker, J. P.; Rantanen, J.; Arnfast, L.; Doreth, M.; Raijada, D.; Loebmann, K.; Madsen, C.; Khan, J.; Rades, T.; Müllertz, A.; Hawley, A.; Thomas, D.; Boyd, B. J. Anhydrate to hydrate solid-state transformations of carbamazepine and nitrofurantoin in biorelevant media studied in situ using time-resolved synchrotron X-ray diffraction. *Eur. J. Pharm. Biopharm.* **2016**, *100*, 119–127.
- (21) Connor, E. M.; Sperling, R. S.; Gelber, R.; Kiselev, P.; Scott, G.; O'Sullivan, M. J.; VanDyke, R.; Bey, M.; Shearer, W.; Jacobson, R. L.; Jimenez, E.; O'Neill, E.; Bazin, B.; Delfraissy, J.-F.; Culnane, M.; Coombs, R.; Elkins, M.; Moye, J.; Stratton, P.; Balsley, J. Reduction of Maternal-Infant Transmission of Human Immunodeficiency Virus Type 1 with Zidovudine Treatment. N. Engl. J. Med. 1994, 331 (18), 1173—1180.
- (22) Lai, C.-L.; Gane, E.; Liaw, Y.-F.; Hsu, C.-W.; Thongsawat, S.; Wang, Y.; Chen, Y.; Heathcote, E. J.; Rasenack, J.; Bzowej, N.; Naoumov, N. V.; Di Bisceglie, A. M.; Zeuzem, S.; Moon, Y. M.; Goodman, Z.; Chao, G.; Constance, B. F.; Brown, N. A. Telbivudine versus Lamivudine in Patients with Chronic Hepatitis B. N. Engl. J. Med. 2007, 357 (25), 2576–2588.
- (23) Gerdil, R. The crystal structure of thymine monohydrate. *Acta Crystallogr.* **1961**, *14*, 333–344.
- (24) Perrier, P.; Byrn, S. R. Influence of crystal packing on the solid-state desolvation of purine and pyrimidine hydrates: loss of water of crystallization from thymine monohydrate, cytosine monohydrate, 5-nitrouracil monohydrate, and 2'-deoxyadenosine monohydrate. *J. Org. Chem.* **1982**, 47 (24), 4671–4676.
- (25) Braun, D. E.; Gelbrich, T.; Wurst, K.; Griesser, U. J. Computational and Experimental Characterization of Five Crystal Forms of Thymine: Packing Polymorphism, Polytypism/Disorder, and Stoichiometric 0.8-Hydrate. *Cryst. Growth Des.* **2016**, *16* (6), 3480–3496.
- (26) Hulme, A. T.; Price, S. L. Toward the Prediction of Organic Hydrate Crystal Structures. *J. Chem. Theory Comput.* **2007**, 3 (4), 1597–1608.
- (27) Khawam, A.; Flanagan, D. R. Solid-State Kinetic Models: Basics and Mathematical Fundamentals. *J. Phys. Chem. B* **2006**, *110* (35), 17315–17328.
- (28) Galwey, A. K. Structure and order in thermal dehydrations of crystalline solids. *Thermochim. Acta* **2000**, 355, 181–238.
- (29) Chupas, P. J.; Chapman, K. W.; Kurtz, C.; Hanson, J. C.; Lee, P. L.; Grey, C. P. A versatile sample-environment cell for nonambient X-ray scattering experiments. *J. Appl. Crystallogr.* **2008**, *41*, 822–824.
- (30) Toby, B. H.; Von Dreele, R. B. GSAS-II: the genesis of a modern open-source all purpose crystallography software package. *J. Appl. Crystallogr.* **2013**, *46* (2), 544–549.
- (31) Coelho, A. TOPAS and TOPAS-Academic: an optimization program integrating computer algebra and crystallographic objects written in C++. *J. Appl. Crystallogr.* **2018**, *51* (1), 210–218.
- (32) Khawam, A.; Flanagan, D. R. Basics and Applications of Solid-State Kinetics: A Pharmaceutical Perspective. *J. Pharm. Sci.* **2006**, *95* (3), 472–498.
- (33) Khawam, A.; Flanagan, D. R. Role of isoconversional methods in varying activation energies of solid-state kinetics: I. isothermal kinetic studies. *Thermochim. Acta* **2005**, 429 (1), 93–102.
- (34) Koradia, V.; de Diego, H. L.; Elema, M. R.; Rantanen, J. Integrated Approach to Study the Dehydration Kinetics of Nitro-furantoin Monohydrate. *J. Pharm. Sci.* **2010**, *99* (9), *3966*–*3976*.
- (35) Zhou, D.; Schmitt, E. A.; Zhang, G. G.; Law, D.; Wight, C. A.; Vyazovkin, S.; Grant, D. J. Model-free treatment of the dehydration kinetics of nedocromil sodium trihydrate. *J. Pharm. Sci.* **2003**, 92 (7), 1367–1376.

- (36) Friedman, H. Kinetics of thermal degradation of char-forming plastics from thermogravimetry. Application to a phenolic plastic. *J. Polym. Sci., Part C: Polym. Symp.* **1964**, *6*, 183–195.
- (37) Braun, D. E.; Koztecki, L. H.; McMahon, J. A.; Price, S. L.; Reutzel-Edens, S. M. Navigating the Waters of Unconventional Crystalline Hydrates. *Mol. Pharmaceutics* **2015**, *12* (8), 3069–3088.
- (38) Vippagunta, S. R.; Brittain, H. G.; Grant, D. J. W. Crystalline solids. *Adv. Drug Delivery Rev.* **2001**, *48* (1), 3–26.
- (39) Vogt, F. G.; Brum, J.; Katrincic, L. M.; Flach, A.; Socha, J. M.; Goodman, R. M.; Haltiwanger, R. C. Physical, Crystallographic, and Spectroscopic Characterization of a Crystalline Pharmaceutical Hydrate: Understanding the Role of Water. *Cryst. Growth Des.* **2006**, *6* (10), 2333–2354.
- (40) Guinier, A.; Bokij, G. B.; Boll-Dornberger, K.; Cowley, J. M.; Durovic, S.; Jagodzinski, H.; Krishna, P.; de Wolff, P. M.; Zvyagin, B. B.; Cox, D. E.; Goodman, P.; Hahn, T.; Kuchitsu, K.; Abrahams, S. C. Nomenclature of polytype structures. Report of the International Union of Crystallography Ad hoc Committee on the Nomenclature of Disordered, Modulated and Polytype Structures. *Acta Crystallogr., Sect. A: Found. Crystallogr.* 1984, 40 (4), 399–404.
- (41) Horike, S.; Shimomura, S.; Kitagawa, S. Soft porous crystals. *Nat. Chem.* **2009**, *1* (9), 695–704.
- (42) Canivet, J.; Fateeva, A.; Guo, Y.; Coasne, B.; Farrusseng, D. Water adsorption in MOFs: fundamentals and applications. *Chem. Soc. Rev.* **2014**, 43 (16), 5594–5617.
- (43) Burtch, N. C.; Jasuja, H.; Walton, K. S. Water Stability and Adsorption in Metal—Organic Frameworks. *Chem. Rev.* **2014**, *114* (20), 10575–10612.
- (44) Serre, C.; Millange, F.; Thouvenot, C.; Noguès, M.; Marsolier, G.; Louër, D.; Férey, G. Very Large Breathing Effect in the First Nanoporous Chromium(III)-Based Solids: MIL-53 or CrIII(OH)-{O2C-C6H4-CO2}-{HO2C-C6H4-CO2H}x·H2Oy. *J. Am. Chem. Soc.* 2002, 124 (45), 13519–13526.
- (45) Barnett, S. A.; Hulme, A. T.; Issa, N.; Lewis, T. C.; Price, L. S.; Tocher, D. A.; Price, S. L. The observed and energetically feasible crystal structures of 5-substituted uracils. *New J. Chem.* **2008**, 32 (10), 1761–1775.